From atmospheric corrosive attack to crack propagation for A1N railway axles steel under fatigue: Damage process and detection

Stefano Beretta [a,*], Antonietta Lo Conte [a], John Rudlin [b], Dorothee Panggabean [b]

[a] *Politecnico di Milano, Dept of Mechanical Engineering, via La Masa 1, 20154 Milano, Italy*
[b] *TWI Ltd., Granta Park, Abington, Cambridge CB21 6AL, UK*

Available online 27 August 2014

1. Introduction

Localized corrosive attack due to the electrochemical action of atmospheric agents, onto the surface of uncoated axles or corresponding to damaged zones of the coating for coated axles, are often found at the maintenance inspections. It is likely that failures in railway axles, due to fatigue cracks initiated at corrosion pits, have been the cause of recent railway accidents both in Europe and North America [1,2], the degradation due to corrosion shown by railway axles has increasingly become an area of concern. It is incumbent upon the scientific research to assist the railway industry in developing an operative protocol to prevent corrosion pit triggering of fatigue crack effectively.

Previous research [3–5] has provided some knowledge about the effects of atmospheric corrosion on fatigue properties of A1N steel. The interaction of cyclic load and corrosive environment promotes the pitting, and corrosion pits, in turn, acting as geometrical discontinuities, lead to nucleation of a consistent number of small cracks. The crack growth rate of these small cracks is higher than the crack growth rate in air. The synergistic effect of fatigue and atmospheric corrosion results in a considerable decrease in the fatigue life of the material, and in the suppression of the fatigue limit in the SN diagram.

However, most of the studies on the failure of railway axle mainly concentrate on the mechanical causes and more specifically, fatigue related phenomena. In-service degradation and damage mechanisms of axle steels, such as environmental corrosion and corrosion fatigue, has not yet been investigated with the same detail as fatigue properties in air. The possibility that pitting corrosion found on some areas of the axles and the possibility that the pits caused by the atmospheric corrosive

* Corresponding author.
E-mail addresses: stefano.beretta@polimi.it (S. Beretta), antonietta.loconte@polimi.it (A. Lo Conte), john.rudlin@twi.co.uk (J. Rudlin), dorothee.panggabean@twi.co.uk (D. Panggabean).

Nomenclature

α	scale parameter of the length distribution
γ	shape parameter of the length distribution
μ	minimum crack length
β	parameter of the crack growth model
σ_y	monotonic yield strength
σ_U	ultimate tensile strength
$\sigma_{y,cyc0.2}$	0.2% cyclic proof stress
$\sigma_{y,cyc0.5}$	0.5% cyclic proof stress
ΔS	stress amplitude
$\Delta S_{lim,axle}$	axle fatigue limit
$\Delta S_{design,EN}$	design fatigue limit according to EN standard
$\Delta S_{design,BASS}$	design fatigue limit according to BASS standard
B	parameter of the crack growth model
E_{cyc}	cyclic elastic modulus
H'	Ramberg–Osgood parameter
N	number of cycles
N_f	number of cycles to corrosion fatigue failure
N_{prop}	number of cycles for crack propagation to failure
R	stress ratio
l	circumferential crack length
l_0	Initial crack length
l_f	final crack length
n'	Ramberg–Osgood parameter
n	parameter of the corrosion–fatigue crack growth model

Acronyms

FT	tests to failure
IT	interrupted and not restarted tests
RT	interrupted and restarted tests

attack can promote the nucleation and the subsequent propagation of fatigue cracks had not been considered in earlier studies when defining axles' fatigue properties (Snell [6], Beretta et al. [7]) and crack growth in railway axles (Zerbst et al. [8]).

The lack of a proper discussion and knowledge about the effects of corrosion on axle service durability is due to the absence of a reliable and widely applicable detection method for 'measuring' the corrosion fatigue damage, since current inspection methods designed for crack detection typically do not attempt to identify or measure the corrosion.

For corrosion assessment generally there are a number of standards (NACE [9]) for the measurement and classification of pits, but these are not related to high cycle fatigue level of the axle damage [10,11]. For corrosion fatigue of axles, some results from the application of eddy-currents for the measurement of small cracks induced by corrosion–fatigue are reported in [12,13].

This paper reports the main results about the corrosion fatigue of A1N steel for railway axles, obtained in the framework of the EU founded Wolaxim project [14]. The project has been devoted to broaden the knowledge in fatigue crack initiation and growth in railway axle steels, accounting for the detrimental effect of the slightly corrosive atmospheric environment. The objective has been to develop and recommend a new inspection methodology for corroded railway axles, also supported by a previously proposed predictive model for the assessment of the corrosion fatigue life of the A1N steel for railway axles [4]. In particular attention has been focused onto a procedure able to detect the presence of corrosion–fatigue micro-cracks which could be implemented without dismantling of the wheel set.

The paper describes the different phases of the research that was initially devoted to corrosion–fatigue tests for complementing the previous experimental campaigns (Section 2). The new experiments consisted in a detailed investigation (onto specimens observed at different fatigue lives) of the pit and damage formation (Sections 3). These observations supported the development of a new NDT method (axle surface cleaning and preparation, microscope and scanner, software for image post-processing) for measuring the length of surface micro-cracks (Section 4). The application of a short crack growth model has then proved the ability of the method to identify the first stages of corrosion–fatigue damage (Section 5).

2. Material and experimental procedures

A1N is a normalized 0.35% carbon steel, widely used in the manufacture of railway axles: the matrix consists of a ferritic–pearlitic microstructure with a 20–40 μm ferrite grain size. Its basic mechanical properties are: ultimate tensile strength

σ_U = 597 MPa and monotonic yield strength σ_y = 395 MPa. Cyclic properties are as follows: 0.2% cyclic proof stress $\sigma_{y,cyc0.2}$ = 357 MPa, 0.05% cyclic proof stress $\sigma_{y,cyc0.05}$ = 289 MPa. The parameters of the cyclic Ramberg–Osgood relationship are equal to E_{cyc} = 209,303 MPa, n' = 0.150395 and H' = 907.34 MPa.

According to current axle design standards (EN13103 [15] and EN13104 [16]) the characteristic strength for A1N is $\Delta S_{lim,axle}$ = 400 MPa: the design strength (considering a safety factor of 1.2) is $\Delta S_{design,EN}$ = 332 MPa for axles with 'adequate corrosion protection' and a further reduction to 60% has be considered for the axles with no corrosion protection (EN13261 [17]). Another important reference are the British Standards BASS 503/4 BR [18,19], now superseded by the EN standards, that prescribed a design stress level $\Delta S_{design,BASS}$ = 220 MPa to allow for corrosion effects.

2.1. Small scale experiments

In order to investigate the evolution of the corrosion fatigue damage of A1N steel a series of corrosion–fatigue tests were carried out onto small scale specimen with test conditions similar to the ones already adopted by the authors in [4]. Specimens were hourglass shaped with a minimum diameter of 10 mm. After machining, they were polished up to #1000 grit emery paper and then mirror polished with diamond paste.

Tests were run at $R = -1$, using a four point rotating bending machine (capacity of 35 N m) at a frequency of 10 Hz, Even if results in the literature [20,21] show a significant effect of frequency onto crack growth rate under corrosion–fatigue, we have chosen this value since it corresponds to an average train speed of 100 km/h.

The stress levels of corrosion–fatigue experiments were in the range ΔS = 140–400 MPa: this range has been chosen since it includes the previously mentioned design strength levels indicated by the EN and BASS standards.

Corrosion conditions were continuously applied to specimens by means of a dedicated dropping system with a dripping flow rate of 80 cc/min (Fig. 1a). The artificial rainwater solution [22], characterized by pH = 6, was formulated as follows: ammonium sulfate 46.2 mg/dm^3, sodium sulfate 31.95 mg/dm^3, sodium nitrate 21.25 mg/dm^3 and sodium chloride 84.85 mg/dm^3. During the test, the open circuit potential is measured between the working electrode (WE, specimen) and the reference electrode (RE, argenthal Ag/AgCl), according to the diagram shown in Fig. 1b, [23].

Three types of tests have been carried out:

(i) *Complete corrosion–fatigue tests:* these tests were aimed at complementing previous experiments [4] and obtaining the S–N diagram under corrosion–fatigue especially at low ΔS levels.

(ii) *Interrupted corrosion–fatigue tests for determining the evolution of surface damage:* some tests were interrupted before failure and the corroded surface of the specimen has been chemically cleaned for rust removal to observe it under SEM. Corrosion–fatigue damage has been investigated by collecting data about the number and the size of pits/cracks in a representative area of the specimen surface, at different stress levels and at different fatigue life stages. Data were collected by taking SEM images of a 9 mm^2 corroded area, centered on the minimum diameter of the specimen. Some of the specimens have been sectioned, etched with 2% Nital to reveal the initial pit development. A summary of these tests is reported in Table 1.

(iii) *Tests for determining small crack growth rate:* some corrosion fatigue tests were dedicated to measuring the growth rate of surface cracks. In this case, at regular intervals tests were stopped, the oxide (in a area of about 5 × 5 mm^2) was mechanically removed and plastic replicas of the specimen surface were taken. The length of growing cracks was subsequently measured with an optical microscope. In order to clearly identify the different cracks onto the replicas, two microholes of 100 μm diameter had been drilled onto the specimen surface before the corrosion–fatigue test. Tests were especially carried out at stress levels ΔS = 240 MPa and ΔS = 180 MPa, in order to complement the growth rate dataset previously obtained in [4].

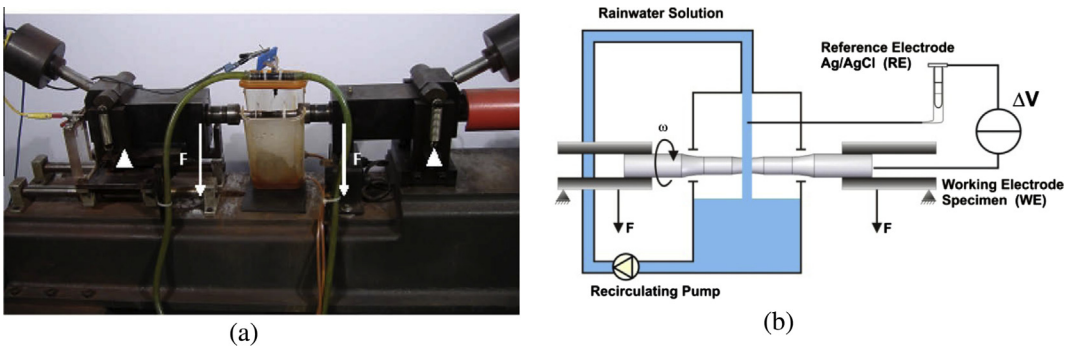

Fig. 1. (a) Set up of the corrosion fatigue experiments. (b) Schematic drawing for corrosion potential measurements [4].

Table 1
Summary of corrosion fatigue interrupted tests (IT).

Test	ΔS (MPa)	Cycles	Life (%)	Stage of the surface damage
IT1	400	1×10^5	7	Only corrosion pits
IT2	400	2×10^5	14	Pits and small cracks
IT3	400	3×10^5	21	Small cracks
IT4	400	4×10^5	28	Long cracks appear
IT5	400	5×10^5	35	Short and long cracks
IT6	400	6×10^5	42	Short and long cracks
IT7	400	7×10^5	49	Short and long cracks
IT8	400	8×10^5	56	Long cracks
IT9	320	5×10^5	14	Small cracks appear
IT10	320	1×10^6	28	Small and long cracks
IT11	320	1.5×10^6	42	Long cracks
IT12	240	8×10^5	6	Pits and small cracks
IT13	240	2×10^6	16	Long cracks appear
IT14	240	6×10^6	47	Long cracks
IT15	180	8×10^5	2	Only corrosion pits
IT16	180	2×10^6	5	Pits and small cracks
IT17	180	5×10^6	11	Small and long cracks
IT18	180	10×10^6	23	Small and long cracks
IT19	140	8.5×10^6	7	Only corrosion pits

2.2. Full-scale fatigue tests

Some full-scale tests were carried out in order to check if the corrosion–fatigue damage was similar to the one observed on small test pieces. The full-scale specimens are hourglass shaped axles with a minimum diameter of 160 mm that are tested onto '3-point rotating bending' test bench with a capacity of 250 kN m, working at its maximum frequency of 8.5 Hz. [24] (there is a small, yet acceptable, difference in frequency with respect to small scale specimens).

The fatigued full scale specimens have been used for setting-up the optical device for corrosion–fatigue damage detection and for testing its crack measurement resolution.

3. Results of the corrosion fatigue experiments

The results of the complete and interrupted fatigue tests are shown in Fig. 2 together with test results from previous research projects. In terms of the S–N diagram, it can be clearly seen that the rainwater corrosion has a significant influence on the fatigue life of A1N. Failures, with $N_f > 10^7$ cycles, also occurred at $\Delta S = 240$ MPa which corresponds to approx. 50% of the fatigue limit in air and the test run at $\Delta S = 140$ MPa also shows a failure at 1.1×10^8 cycles (the test lasted for approx. 20 weeks).

At low stress levels, below the air fatigue limit of the material (fatigue limit $\Delta S = 510$ MPa [3]), the presence of a corrosive environment allows crack nucleation, from corrosion pits, and enables the growth of small cracks that would have not been able to propagate in air. This process results in a disappearance of the air fatigue limit and in a continuously decreasing S–N diagram in the corrosive environment. In the following the different phases of the process (shown as a sequence of observations at $\Delta S = 400$ MPa Fig. 3) will be discussed in the next subsections.

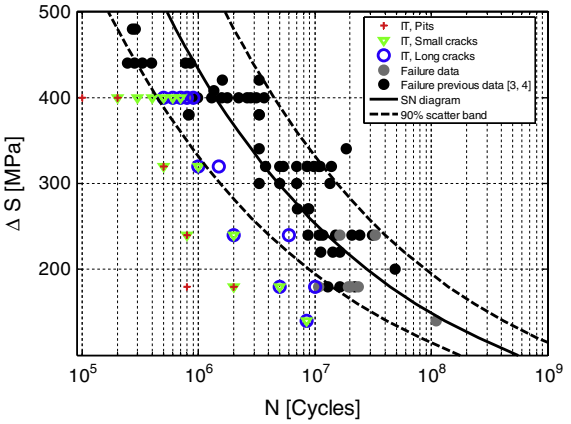

Fig. 2. Corrosion fatigue SN diagram completed with interrupted tests at different stage of the rupture life.

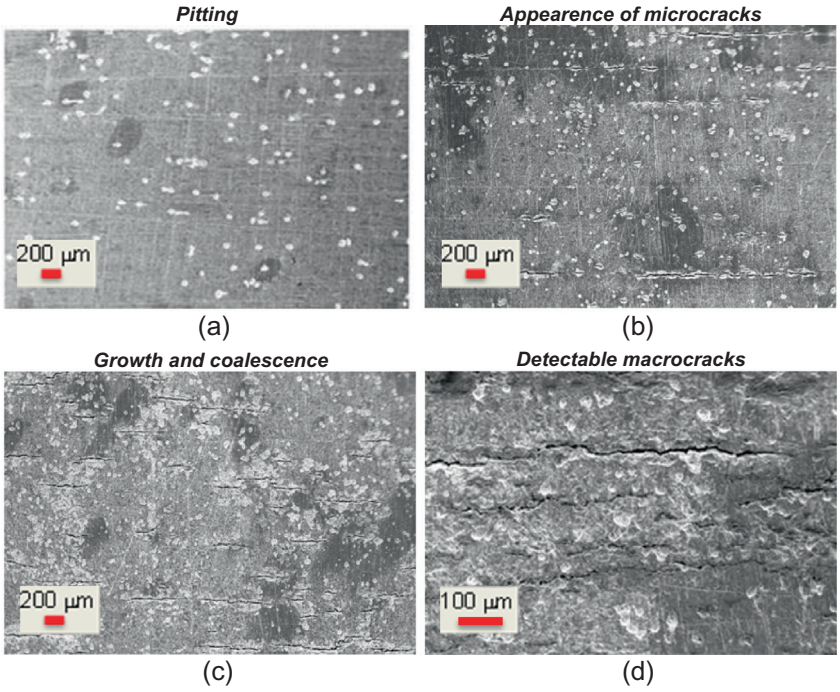

Fig. 3. Surface of specimens tested at $\Delta S = 400$ MPa, interrupted at different number of cyles: (a) IT1 10^5 cycles (7% life); (b) IT2 2×10^5 cycles (14% life); (c) IT4 4×10^5 cycles (28% life); (d) IT8 8×10^5 cycles (56% life).

3.1. Corrosion pit formation

The initiation and growth characteristic of the corrosion pits were investigated by observation of interrupted tests in the early stage of the corrosion fatigue cracking. Fig. 4a shows the corroded surface of the specimens at $\Delta S = 400$ MPa and interrupted after only 1×10^5 cycles which correspond to 7% of corrosion–fatigue life. After the mechanical cleaning, the surface of the specimen presents rather uniformly generated corrosion pits (Fig. 4b and c).

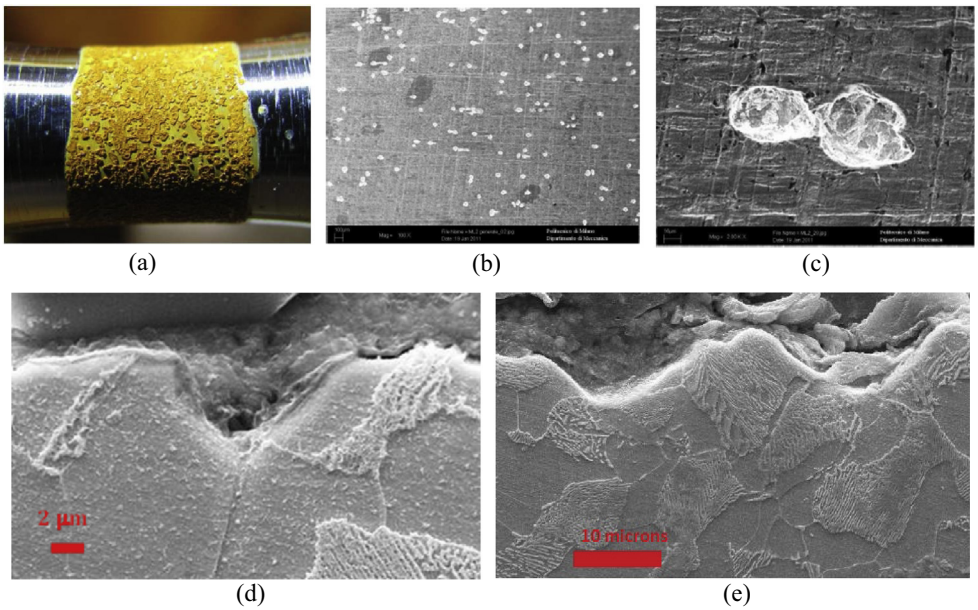

Fig. 4. Specimen at $\Delta S = 400$ MPa and interrupted after only 1×10^5 cycles: (a) corroded surface; (b) randomly generated corrosion pits; (c) detail of two corrosion pits. (d) Sectional image of corrosion pits nucleated at the ferrite–ferrite grain boundary; (e) sectional image of corrosion pits encompassed by pearlite grains.

An attempt to document the preferential locations of the pit nucleation sites has been made. A SEM analysis of the etched cross section of various specimen shows, that apart few pits nucleated at the interface between inclusion and matrix, the nucleation sites in the microstructure are most frequently at the ferrite–ferrite boundary of the grain (Fig. 4d) and the ferrite body grain, rarely also the pearlitic body grain. There is a high occurrence of corrosion pits surrounded by pearlitic grains (Fig. 2e), while no pit nucleation at the ferritic–pearlitic interface has been found.

An interesting characteristic of pits nucleated at the ferrite–ferrite grain boundary is the slightly conical pit profile that can be seen in the same Fig. 4d, while the pits nucleated at the ferrite body grain exhibits initial elliptical shape. In both cases the profile change into more hemispherical one, with increasing exposure time.

The electrochemical behavior of the different phases supports the experimental observations. In fact, the pearlite is electrochemically more stable and exhibits a higher corrosion potential than ferrite, can be expected to be more easily corroded from thermodynamics point of view [25,26]. On the other hand, the high occurrence of pits nucleated at ferrite –ferrite grain boundaries may be due to the segregation of second phases that causes them to be more anodic than the surrounding grains.

After the formation, corrosion pits grow and their growth rate depends on the exposure time and the stress level according to models by Ishihara et al. [20,27] At the same time other pits are newly formed at other locations so that the pit density increases during corrosion fatigue life [28]. Instead of measuring the evolution of pit size, the observations on interrupted tests have been devoted to investigation of the transition from pits to cracks.

3.2. Pit-to-crack transition and crack formation

Fig. 5 shows the surface of a specimen subjected to a interrupted test at $\Delta S = 400$ MPa for 2×10^5 cycles (14% of life). Beside some small cracks, the presence of small pits similar to the ones in Fig. 4b together with many bigger pits at the pit-to-crack transition can be observed.

We have identified three stages of the pit-to-crack transition: they are shown in detail in Fig. 5, where they have been labeled as Type A–B–C respectively. Initially, when the pit depth reaches 15–20 μm, a secondary pit initiates at the bottom of the primary hemispherical pit due to the corrosive attack (stage A). Subsequently, a microcrack starts from the bottom of the primary pit (stage B) and it then grows out of the primary pit (stage C).

The size of the pits at the pit-to-crack transition has been investigated using the specimens of interrupted tests by measuring under SEM, after mechanical and chemical cleaning of the specimen surface, the size of pits at each of the three stages of the pit-to-crack transition (either Type A, B or C) onto a surface of 9 mm^2. No measurements were carried out onto pits below the pit-to-crack transition. Table 2, reports the mean value and standard deviation of the pit diameter for the three stages of pit-to-crack transition observed in the different interrupted tests (no pits in transition were observed in IT1 test). It is worth remarking that the average pit diameter remains approximately the same for the three stages of pit-to-crack transition, as shown in Fig. 6 for the IT2 specimen. This fact confirms that the electrochemical dissolution is concentrated at the bottom of the pit once it has attained a critical size. Moreover, the measurements at different stress levels show that the size of the pits in the three stages do not vary significantly with the stress level (from 25 to 40 μm).

It seems that our observations are contradicting the ones of Turnbull et al. [29,30], who showed a pit-to crack transition characterized by the development of surface cracks. However, Horner et al. [30] have shown that the pit-to-crack transition is driven by plastic strains: at the low stress level of the experiments here presented (S_{max} = 70–200 MPa), plastic strains can only occur at the mouth of secondary pits where there is a very high stress concentration (see Cerit et al. [31]).

This concept of secondary pit growth can then be considered as the factor triggering the transition from pit to corrosion–fatigue crack providing a satisfactory explanation for the three phases pit-to-crack transition experimentally observed (Fig. 5b). On the other hand, it is difficult to exactly calculate a $K_{pit\text{-}to\text{-}crack}$ [32] for the real geometry of primary + secondary pit (the tentative estimation of SIF for propagating cracks on interrupted tests was already done in [4], but it was only pos-sible to estimate a lower bound of $K_{pit\text{-}to\text{-}crack}$). We have therefore preferred, for the sake of life prediction (see Section 5.1), to consider an average diameter of the pit at the pit-to-crack transition of 30 μm.

The other significant observation, from the surface analysis of the specimens interrupted at different stages of the fatigue life, is that only those pits with primary + secondary morphology act as crack initiation sites.

3.3. Crack propagation

The crack growth rate has been measured by means of plastic replica, during interrupted corrosion–fatigue tests. Examples of the images taken with plastic replicas are shown in Fig. 7a: no difference in the growth rate between cracks starting from corrosion pits and cracks nucleated from the drilled holes was observed (as it was already noted in [4]). The crack growth model at the different stress levels (see Fig. 7b) we have adopted is a simplified version of the model described in [4]. In particular, with respect to the previous model [4] which was a modification of the one by Murtaza and Akid [33], we have dropped the term related to a mechanical threshold, since the pit formation appears to be a continuous process con-trolled by a critical pit dimension.

The model describes the corrosion fatigue growth rate of small cracks by means of the following power law equation:

$$\frac{dl}{dN} = B \cdot (\Delta S)^{\beta} \cdot l^{n} \tag{1}$$

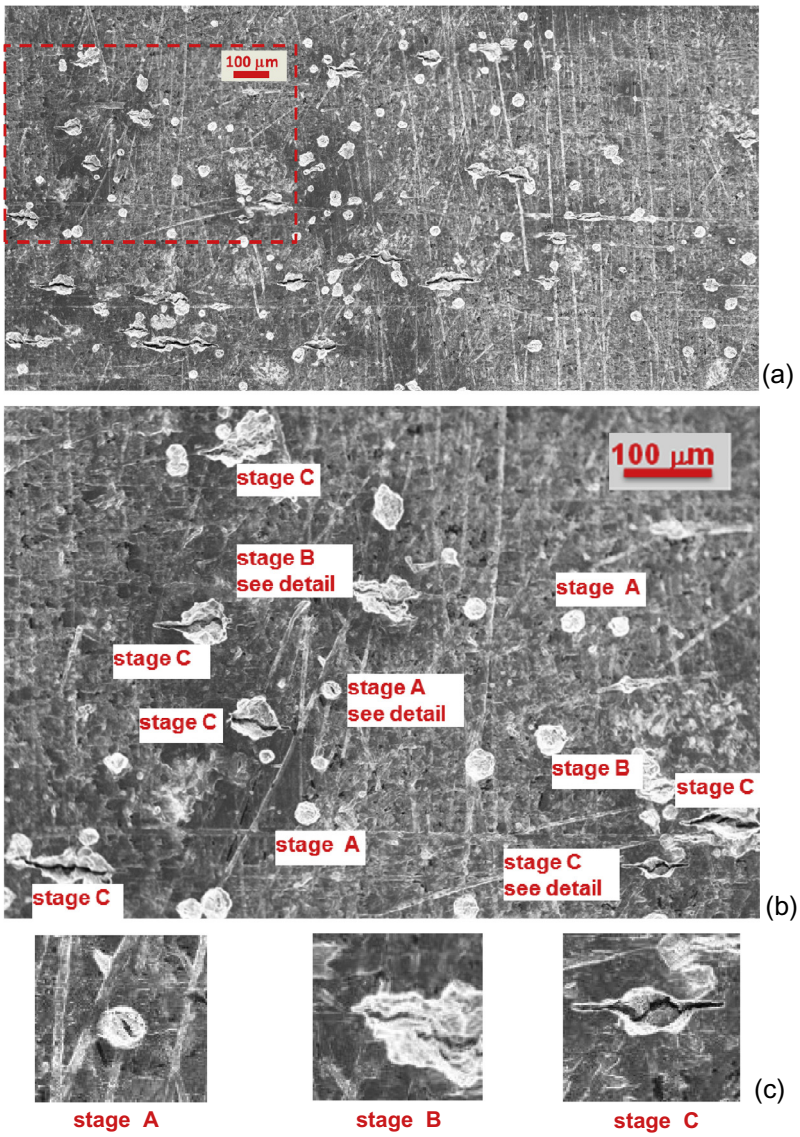

Fig. 5. Surface appearance of the specimen tested at $\Delta S = 200$ MPa interrupted at $N = 2 \times 10^5$ cycles (14% Life); (a) general view with pits and small cracks; (b) detail with pits and three different stages of the pit-to-crack transition; (c) stage A: electrochemical dissolution at the bottom of the surface pit and formation of a secondary pit, stage B: nucleation of a microcrack. Stage C: growth of the crack out of the pit.

Table 2
Mean value and standard deviation of the pit diameter for the three phases of pit-crack transition identified in Fig. 5, as measured onto different interrupted tests.

		$\Delta S = 400$ MPa $N = 2 \times 10^5$ cycles Test IT2		$\Delta S = 400$ MPa $N = 5 \times 10^5$ cycles Test IT5		$\Delta S = 400$ MPa $N = 8 \times 10^5$ cycles Test IT8		$\Delta S = 240$ MPa $N = 8 \times 10^5$ cycles Test IT12		$\Delta S = 180$ MPa $N = 8 \times 10^5$ cycles Test IT15	
		Mean	Std	Mean	Std	Mean	Std	Mean	Std	Mean	Std
Pit	Stage A	30	6	42	8	23	4	41	3	44	15
	Stage B	33	6	28	6	26	3	40	9	/	/
	Stage C	31	7	26	7	25	4	31	4	/	/

where ΔS is the stress range, l is the surface crack length, B, β, and n are material parameters obtained by interpolating propagation data. As it can be seen from Fig. 7b, the model describes very well the data at the different levels and there is no evidence of a 'threshold' in the test data even if we have measured growth rates of the order of 10^{-8} mm/cycle.

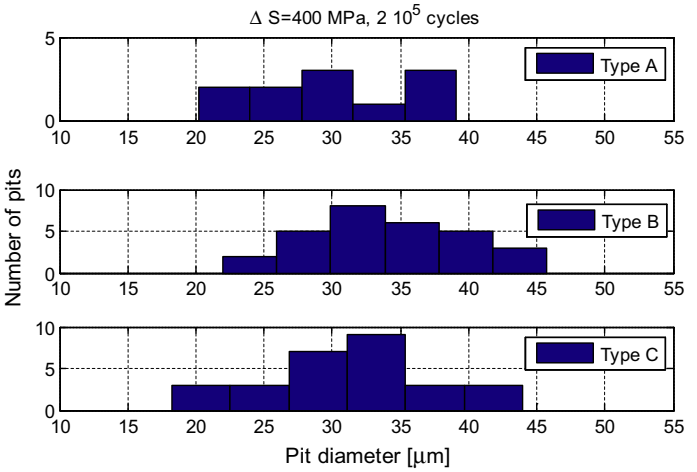

Fig. 6. Histogram of the pits diameter for the three type of pits identified in Fig. 5 for the test at $\Delta S = 400$ MPa interrupted after 8×10^5 cycles. Data pertain to a 9 mm^2 surface.

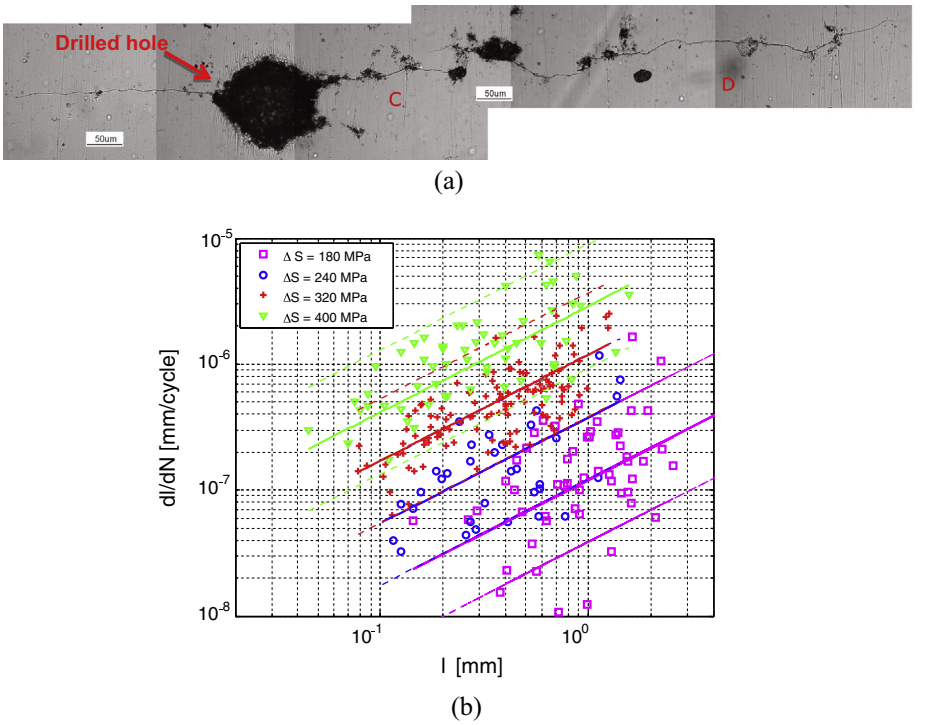

Fig. 7. Crack growth experiments: (a) 2 cracks (labeled as C and D) that have joined together to form a single crack (crack C nucleated from the drilled hole which is visible at the center of the microcrack); (b) crack growth rate at the different stress levels and their interpolation with Eq. (2) (the dashed lines corresponds to 5% and 95% probability).

3.4. Evolution of cracking and damage

Corrosion–fatigue damage was also investigated by collecting data about the number and the circumferential length of cracks onto specimens subjected to interrupted tests. Data were collected by taking SEM images of a 9 mm^2 superficial area, centered on the minimum diameter. The results are reported in Table 3, where it can be seen that during the life the mean crack length is increasing. The number/density of cracks is increasing at the beginning of the life because of growth of new cracks from newly formed pits and it tends to decrease toward the end of the life because of the coalescence into larger cracks. Moreover, the corrosion–fatigue cracks show a peculiar zig–zag patterns that can be clearly observed on Fig. 3c and d.

Table 3
Crack length for unit area and mean crack length at different stage of the corrosion fatigue life (the grey cells corresponds to tests where less than 25% of the cracks have a length above the resolution of the optical device).

		Percentage of life								
		5–7%	11%	14–16%	21–23%	28%	35%	42%	47–49%	56%
ΔS = 400 MPa	Test			IT2	IT3	IT4	IT5	IT6	IT7	IT8
	Cracks density (1/mm^2)			0.76	1.41	1.76	1.86	1.94	2.26	1.5
	Mean length (μm)			171	156	284	246	348	408	411
ΔS = 320 MPa	Test			IT9		IT10		IT11		
	Cracks density (1/mm^2)			0.8		2.87		3.93		
	Mean length (μm)			117		191		287		
ΔS = 240 MPa	Test	IT12		IT13					IT14	
	Cracks density (1/mm^2)	1.4		5.6					3.11	
	Mean length (μm)	82		150					467	
ΔS = 180 MPa	Test	IT16	IT17		IT18					
	Cracks density (1/mm^2)	1.27	2.13		2.34					
	Mean length (μm)	179	352		586					
ΔS = 140 MPa	Test	IT19								
	Cracks density (1/mm^2)	1.94								
	Mean length (μm)	387								

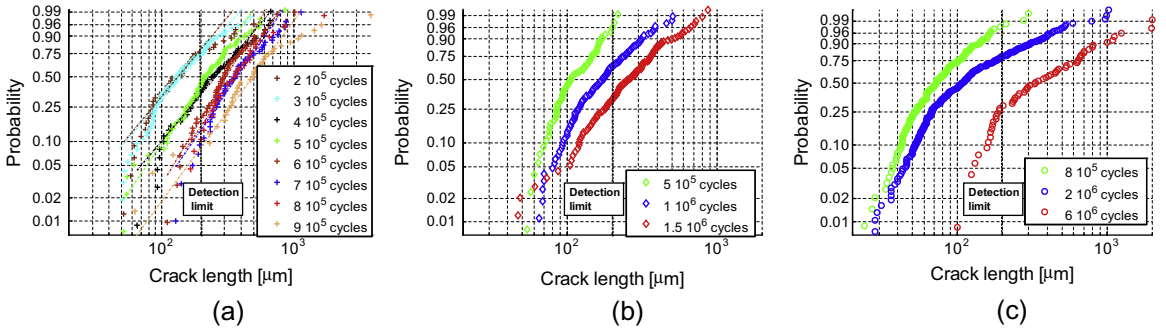

Fig. 8. Weibull plot of the circumferential crack length for the corrosion fatigue test: ΔS = 400 MPa; (b) ΔS = 320 MPa; c) ΔS = 240 MPa.

Fatigue damage is in general monitored trough the analysis of the distribution of surface cracks [34,35] with the Weibull distribution, characterized by a distribution function:

$$F(l) = 1 - \exp\left[-\left(\frac{l-\mu}{\alpha}\right)^{\gamma}\right] \tag{2}$$

where α, γ respectively are the scale and shape parameters and μ is the minimum crack length.

The evolution of the distribution of surface cracks along the life can be appreciated from Fig. 8, where the crack length data are plotted onto Weibull probability paper: it can be clearly appreciated the 'mouvement' of the distribution due to crack growth and nucleation of new cracks. It is worth remarking that the data in Fig. 8b and c clearly show that, at the different cycles, the data tend to a minimum crack length l_o in the range 35–50 μm (which is close to the dimension of pit-to-crack transition).

We have also marked, onto the probability papers, the line corresponding to a crack length of 200 μm, which is the resolution limit for the field optical inspection equipment made during the Wolaxim project.

4. Optical inspection equipment

As for corrosion fatigue crack initiation and growth, several stages of damage have been shown in the previous sections. Below a certain stage of cracking, the axle is still in an operational condition and its removal from circulation is not required and it can be returned to service without a safety risk.

However this stage is not clearly visible and a surface NDT technique enabling the selection of operational axle should be made available. The NDT technique should quantify the microcrack status or carry out a microscopic evaluation of the surface (or a combination of methods). An optical method was considered, a set of equipment has been selected and software interface aiding the user to quantify the stage of cracking of an axle [36].

The equipment used for the inspection comprised of a microscope, its holder and a scanner (Fig. 9). The holder could place the microscope in an angle which was necessary in order to observe the region at 90° from the surface of the axle when the latter was located on a curved surface (wheel seat for instance). The scanner enabled the user to rotate the microscope all

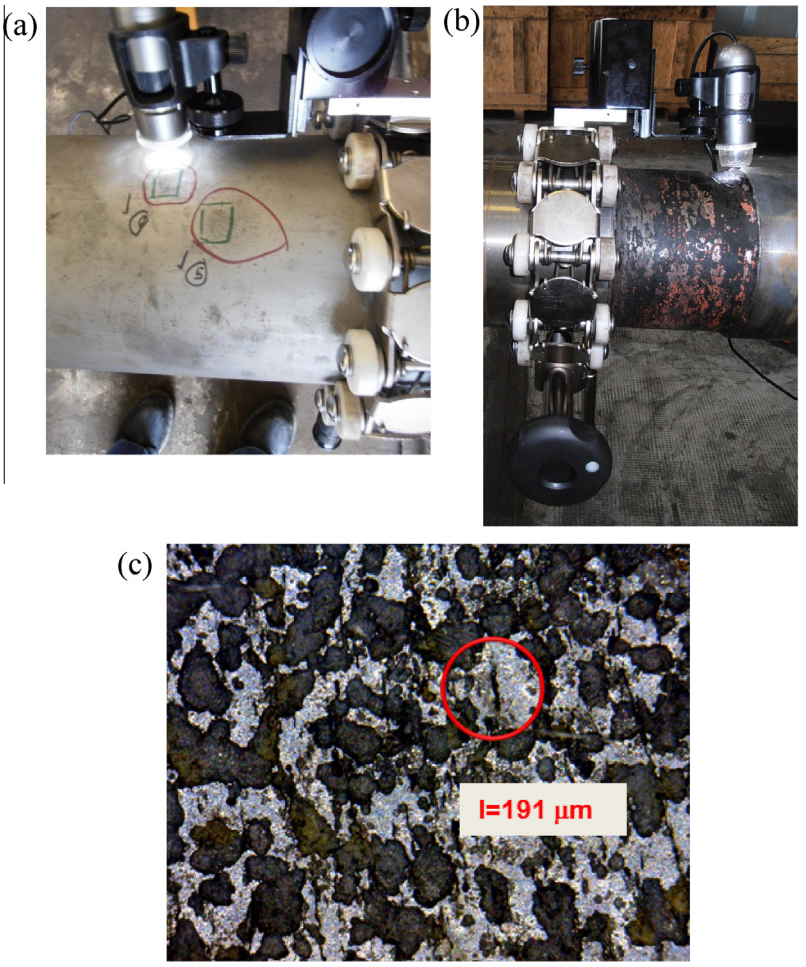

Fig. 9. Optical device for damage detection: (a) the microscope, holder and scanner; (b) deployment in inspection of a full-scale specimen; (c) microcrack detection during a corrosion fatigue test onto a 'full scale' axle specimen.

around the axle in order to inspect the entire circumference. The assembly of the scanner and holder allowed the microscope to be placed in a stable position suitable for inspecting an area and recording images of the inspected area. These were tested in site conditions (Fig. 9a) and during full-scale corrosion fatigue tests (Fig. 9b). The rust on the train axle was removed using a procedure developed in the project since before the inspection it covered the cracked region entirely.

The microscope enabled the user to inspect a potentially cracked region of the axle. In some cases, the microscope with a polarization capability was used in order to highlight the presence of cracks in the axle (see Fig. 9c). Alternatively images could be recorded and processed with software in order to size and quantify the cracks in the inspected region. For recording operations, once appropriate controls have been selected different light bulbs can be activated, together with the polarization in order to have the appropriate lighting on the specimen. As soon as the microscope is in place and the lighting is correct, the image can be captured and then analyzed. A series of comparison with plastic replicas of the full scale axles and SEM images, allowed us to compare the crack length measured with the *on-axle* microscope: the conclusion was that the de-oxidizing procedure and the on-site observations allow the user to accurately detect and measure cracks with a length of the order of 200 μm (Fig. 9c).

The analysis operates by taking an image and selecting part of it. At this stage a threshold is set for the image. Once this has been done the software automatically identifies cracks and pits by their morphological properties (e.g. shape and direction), and then determines their size and counts them. The final outcome is the number of cracks and other objects detected (cracks can be clearly identified by the aspect ratio) and their size: the average length of the detected cracks can then be readily calculated.

4.1. Field measurements

The optical device has been applied to field measurements carried out within the Wolaxim project. A number of axles withdrawn from service at three different sites in the UK were examined using the device. No difficulty was found deploying

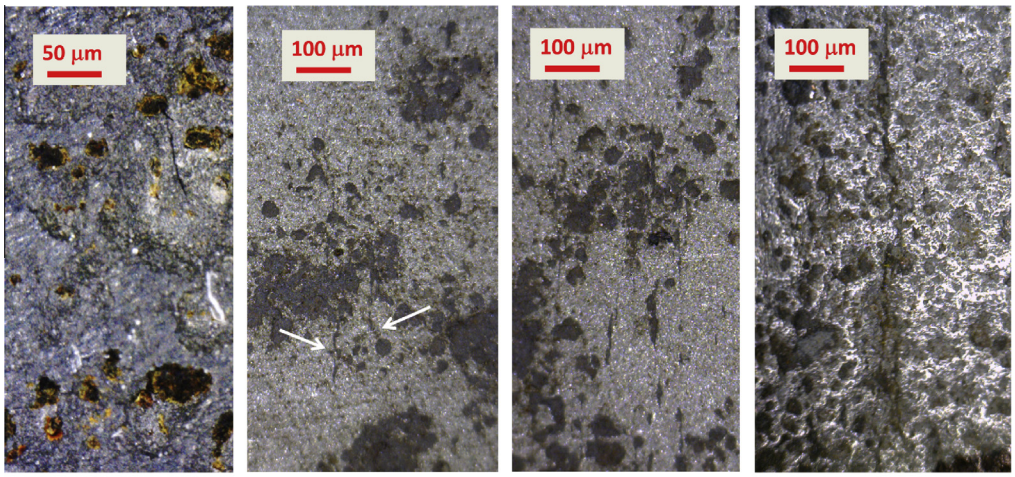

Fig. 10. Examples of different stages of corrosion–fatigue detected on axles retired from service. (a) Trial 1, (b) and (c) Trial 2, (d) Trial 3.

the device in depot or overhaul situations. In the majority of areas examined, no cracks were found indicating that more than 95% of life was left (see Section 5.2). However some cracks were detected as shown in Fig. 10. The evidence of small cracks initiating from pits in the service conditions can be seen, thus verifying that the process observed in the laboratory was also occurring in service. These cracks were isolated and are all under 1 mm in length and indicate that considerable life was left in the axles, although the presence of the cracks in any case suggests that some corrosion–fatigue life had been used up.

5. Corrosion fatigue predictive model

5.1. Life prediction for small scale specimens

By adopting Eq. (1), a description of the S–N diagram in terms of propagation of corrosion fatigue cracks from the transition length from short crack to long crack to the final crack length can be also obtained very easily:

$$N_{prop} = \frac{1}{B \cdot (\Delta S)^{\beta}} \int_{l_o}^{l_f} \frac{dl}{l^{\pi}} \tag{3}$$

where l_o is the initial crack length, corresponding to the average pit size (which was assumed 30 μm for the different stress levels) at the pit-to-crack transition, and l_f was the final crack length corresponding to failure (l_f ranges from 1.5 and to 3 mm respectively for stress levels ΔS = 400 MPa and ΔS = 180 MPa). Fig. 11 shows the corrosion fatigue prediction of the model, according to Eq. (2), compared with experimental fatigue data.

Despite the neglect of the initial pit formation and pit-to-crack processes, the prediction of the corrosion–fatigue life in terms of propagation of small cracks describes the median S–N diagram fairly accurately due to the very rapid crack formation process.

5.2. Validity of the optical NDT

The crack growth equations can be also used for verifying the applicability of the detection procedure based onto the on-axle microscope. If we integrate Eq. (2) adopting l_f = 200 μm which corresponds to the crack length that can be measured with the device, and the growth rate corresponding to 95% percentile, then we can obtain a conservative estimate the portion of the fatigue process below the detection resolution. This area, labeled as 'no detection' is also shown in Fig. 11. In the same graph the measurements on IT specimens were a significant proportion (at least 25%) of the cracks was longer than 200 μm are labeled as *'positive detections'*: it can be seen that the earliest detections are close to the curve for 5% failure probability.

The conclusion that we have drawn is the NDT method here proposed (cleaning procedure, on-axle optical measurements, post processing of the surface images) can effectively detect the early stages of the corrosion–fatigue process. A series of full-scale axle tested at different stress levels have been run to validate the applicability in situ of the proposed detection method.

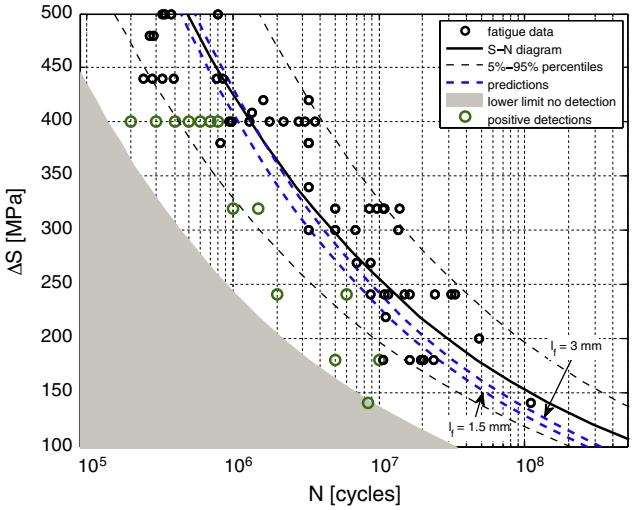

Fig. 11. Prediction of S–N diagram under corrosion fatigue (l_f = 1.5 mm and l_f = 3 mm) and prediction of the region where damage cannot be observed with the optical device (l_f = 0.2 mm).

6. Conclusion

Atmospheric corrosion has a significant influence on the A1N fatigue life. When atmospheric corrosion is present the SN diagram shows a dramatic reduction of fatigue life with the appearance of corrosion fatigue cracks widespread onto the corroded surface that could be taken as an indicator of damage.

The morphology and the time-evolution of the corrosion–fatigue damage have been deeply investigated. The pit-to-crack transition occurring in the very early stage of the corrosion fatigue damage, approximately within the 5% of the average life, is characterized by the formation of secondary pits triggering the formation of small cracks. After this early formation, the crack growth is characterized by a zig–zag path due to the coalescence of single cracks propagating on different microstructural planes.

A prototype of an optical equipment set on the basis of the new acquired knowledge has been proposed and its application to detect corrosion fatigue micro-cracks, onto the surface of railway axles in situ conditions, has been successful reported. The application of a short crack growth model has then proved the ability of the method to identify the first stages of corrosion–fatigue damage.

Acknowledgements

This work was funded by the European Union under the FP7 Capacities programme Grant Agreement No FP7-SME-2010-1-262442 monitored by the Research Executive Agency (REA). The support and permission of the other partners in the project (BAM – Germany, Applied Inspection – UK, CGM – Italy, Diatek – Germany, RCP – Germany, Lucchini – UK, ATM – Italy) is gratefully acknowledged.

References

[1] Hoddinott DS. Railway axle failure investigations and fatigue crack growth monitoring of an axle. Proc Instn Mech Eng Part F: J Rail Rapid Transit 2004;218:283–92.
[2] Transportation Safety Board of Canada. Main track derailment: Canadian national train no. G-894-31-14. Railway Investigation Report R01Q0010; 2001.
[3] Beretta S, Carboni M, Lo Conte A, Palermo E. An investigation of the effects of corrosion on the fatigue strength of AlN axle steel. Proc Inst Mech Eng Part F J Rail Rapid Transit 2008;222:129–43.
[4] Beretta S, Carboni M, Fiore G, Lo A. Conte, corrosion–fatigue of A1N railway axle steel exposed to rainwater. Int J Fatigue 2010;32:952–61.
[5] Moon A, Sangal S, Mondal K. Corrosion behaviour of new railway axle steels. Trans Indian Inst Met 2013;66(1):33–41. http://dx.doi.org/10.1007/s12666-012-0167-0.
[6] Snell JR. Key issues in the application of unified railway axle standards. Proc Inst Mech Eng Part F: J Rail Rapid Transit 2004;218:279–82.
[7] Beretta S, Ghidini A, Lombardo F. Fracture mechanics and scale effects in the fatigue of railway axles. Eng Fract Mech 2005;72:195–208.
[8] Zerbst U, Vormwald M, Andersch C, Mädler K, Pfuff M. The development of a damage tolerance concept for railway components and its demonstration for a railway axle. Eng Fract Mech 2005;72:209–39.
[9] Baboian R, editor. Nace corrosion engineer's reference book. Houston: NACE International; 2002.
[10] Lin Chih-Kuang, Lan I-Lon. Fatigue behavior of AISI 347 stainless steel in various environments. J Mater Sci 2004;39:6901–8.
[11] Turnbull A, McCartneey LN, Zhou S. Modelling of evolution of stress corrosion cracks from corrosions pits. Scripta Mater 2006;54:575–8.
[12] Carboni M, Beretta S, Lo Conte SA. Research on corrosion fatigue of railway axles. Insight: Non-Destruct Testing Condit Monit 2011;53(7):361–7.

[13] Carboni M. Application of eddy currents to the inspection of fatigue corroded railway axles. In: Proceedings of 18th world conference on nondestructive testing. Durban, South Africa; 16–20 April 2012.
[14] <http://www.wolaxim.eu>.
[15] EN13103:2001 Railway applications. Wheelsets and bogies. Non-powered axles. Design method.
[16] EN13104:2001 Railway applications. Wheelsets and bogies. Powered axles. Design method.
[17] BS EN13261:2009+A1 2010 Railway applications. Wheelsets and bogies. Axles. Product requirements.
[18] BR-BASS503. Design guide for the calculation of stresses in driving axles. Railway Companies of 1996, Issue C, 1996.
[19] BR-BASS504. Design guide for the calculation of stresses in non-driving axles. Railway Companies of 1996, Issue C, 1996.
[20] Ishihara S, Saka S, Nan ZY, Goshima T, Sunada S. Prediction of corrosion fatigue lives of aluminium alloy on the basis of corrosion pit growth law. Fatigue Fract Eng Mater Struct 2006;29:472–80.
[21] Miller KJ, Akid R. The application of microstructural fracture mechanics to various metal surface states. Proc R Soc Lond A 1996;452:1411–32.
[22] Brunoro G, Frignani A, Colledan A, Chiavari C. Organic films for protection of copper and bronze against acid rain corrosion. Corros Sci 2003;45:2219–31.
[23] Leinenbach C, Fleck C, Eifler D. The cyclic deformation behavior and fatigue induced damage of the implant alloy TiAl6Nb7 in simulated physiological media. Int J Fatigue 2004;26:857–64.
[24] Beretta S, Carboni M, Lo Conte A, Regazzi D, Trasatti S, Rizzi M. Crack growth studies in railway axles under corrosion fatigue: Full-scale experiments and model validation. Proc Eng 2011;10:3650–5.
[25] Qu Shaopeng, Pang Xiaolu, Wang yanbin, Gao Kewei. Corrosion behavior of each phase in low carbon microalloyed ferrite–bainite dual-phase steel: experiments and modeling. Corros Sci 2013;75:67–77.
[26] Du CW, Li XG, Liang P, Liu ZY, Jia GF, Cheng YF. Effect of microstructure on corrosion of X70 pipe steel in an alkaline soil. J Mater Eng Perform 2009;18:216–20.
[27] Vignal V, Mary N, Valot C, Oltra R, Coudreuse L. Electrochem Solid-State Lett 2004;7(4):C39–42.
[28] Pidaparti RM, Patel RK. Investigation of a single pit/defect evolution during the corrosion process. Corros Sci 2010;52:3150–3.
[29] Turnbull A, Horner DA, Connolly BJ. Challenges in modelling the evolution of stress corrosion cracks from pits. Eng Fract Mech 2009;76:633–40.
[30] Horner DA, Connolly BJ, Zhou S, Crocker L, Turnbull A. Novel images of the evolution of stress corrosion cracks from corrosion pits. Corros Sci 2011;53:3466–85.
[31] Cerit M, Genel K, Eksi S. Numerical investigation on stress concentration of corrosion pit. Eng Failure Anal 2009;16(7):2467–72.
[32] Kondo Y. Prediction of fatigue crack initiation life based on pit growth. Corrosion 1989;45(1):7–11.
[33] Murtaza G, Akid R. Empirical corrosion fatigue life prediction for a high strength steel. Eng Fract Mech 2000;67:461–74.
[34] Goto M. Statistical investigations of the behavior of micro-cracks in carbon steels. Fatigue Fract Eng Mater Struct 1991;14:833–45.
[35] Beretta S, Clerici P. Micro-crack propagation and micro-structural parameters of fatigue damage. Fatigue Fract Eng Mater Struct 1996;19:1107–15.
[36] Rudlin J, Raude A, Völz U, Lo Conte A. New methods of rail axle inspection and assessment. In: Proceedings of 18th world conference on nondestructive testing. Durban, South Africa; 16–20 April 2012.